

Synthesis of Fe₃O₄/ ZnO/CuO Nanocomposite and its Sono-photocatalyst property for removal of methylene blue from wastewater

Samira Pishkar Ahrab¹, Mahdiyeh pourali², MohammadTaghi Hamedani^{*1},

1. Faculty of Mechanical Engineering, Tabriz University, Tabriz, 51616471, Iran.

2. Faculty of Materials Engineering, Sahand University of Technology, Tabriz, 513351996, Iran.

Abstract

Fe₃O₄/ZnO/CuO nanocomposites with various molar ratios of CuO were successfully synthesized. Sol-gel method was used to synthesize nanocomposite materials at a low temperature. A set of experiments, including X-ray diffraction (XRD), Dynamic Light Scattering (DLS), scanning electron microscopy (SEM), and UV-Vis spectroscopy, was used to confirm the successful synthesis of Fe₃O₄/ZnO/CuO nanocomposites in crystalline form.

The photocatalytic activity of the samples was investigated via the degradation of methylene blue (MB) dye from synthetic wastewater under three distinct conditions: visible light, ultraviolet light, and a combination of visible light with ultrasonic treatment. Fe₃O₄/ZnO/CuO nanocomposite with a molar ratio of 1:1:0.5 showed the highest photocatalytic activity when irradiated with either visible or ultraviolet light. Furthermore, when visible light was combined with ultrasonic treatment, complete (100%) removal of methylene blue was achieved within 120 minutes. The results demonstrate that these nanocomposites are efficient catalysts for wastewater treatment through the removal of organic pollutants.

Keywords Fe₃O₄/ZnO/CuO, Sono-photocatalyst, nanocomposite, Wastewater treatment

1 Introduction

Over the past few decades, there have been some emerging problems in the industry, whereas environmental pollution has attracted a lot of attention in the world [1]. The release of organic dyes from the textile, leather, food, cosmetics, and pharmaceutical industries into the environment has resulted in significant issues for living organisms. Also, water pollution is a problem that should be identified as soon as possible. Researchers have done a great deal of research on how to treat infected water from the processing of industrial products and household waste [2].

Nevertheless, the conventional wastewater treatment method still contains a large number of contaminants that are challenging to eliminate. For instance, antibiotics, dyes, organic insecticides, multi-rheological aromatic hydrocarbons [3-6], etc. New techniques, like Fenton oxidation [7] and a hybrid approach that combines multiple purification processes, like active carbon, biofilm, enzymatic reactors, etc., have been developed to remove these contaminants [8]. These techniques have garnered interest from researchers [9] and have a positive impact on the degradation of contaminated organic matter. Another method for removing

* Corresponding author

Professor of Materials science and engineering, Mechanic faculty, Tabriz university, Tabriz ,Iran.

Email m.hamedani.tabrizu@gmail.com, Tel: +989147618082 & +98-41-33356026, Fax: +98-41-33354153

56 pollutants is to use Semiconducting oxides with
57 photocatalytic properties. Various catalysts
58 have been introduced to remove pollutants or
59 even make them non-irritating chemicals [10].
60 Among them, TiO_2 and ZnO semiconductors
61 have been introduced as successful
62 photocatalysts for the destruction of organic
63 pollutants. The advantages of ZnO
64 nanoparticles include strong oxidizing ability,
65 light sensitivity, excellent mechanical and
66 chemical stability, non-toxic nature, favorable
67 energy gap, and cheap price [11]. However, to
68 use ZnO as a photocatalyst, according to the
69 band gap (3.2 electron volts), it is necessary to
70 use ultraviolet light that only contains less than
71 10% of the sun's light. While in the sunlight,
72 45% of the radiation is visible in the light range
73 [12,13]. To enhance the photocatalytic activity
74 of ZnO under the influence of visible light,
75 solutions need to be considered. The formation
76 of a ZnO nanoparticle composite with other
77 metal oxides results in the absorption of
78 stronger light and increased ability to absorb
79 visible light [14]. In addition, this composite
80 prevents recombining electron-hole and
81 increases the photocatalyst's efficiency [15].
82 The coupling of ZnO with CuO nanoparticles
83 and their composite formation is a promising
84 method for increasing photocatalytic
85 properties. Besides extending the absorption
86 range towards the visible light, this method
87 transmits electrons produced by the photon
88 from a high-conductivity band of CuO to a low-
89 conductivity band of ZnO , which results in the
90 effective separation of the electron-hole [16].
91 So far, considerable research has been done on
92 the synthesis of ZnO / CuO as a special high-
93 level catalyst. Number of techniques have been
94 put up to create a ZnO/CuO catalyst, such as
95 mechanical methods, for example grinding, wet
96 chemistry, coprecipitation, thermal
97 decomposition, sol-gel, hydrothermal, and
98 photo deposition methods [17]. Another
99 problem for catalysts is their segregation from
100 purified water in practical applications.
101 Traditional methods such as coagulation and
102 filtration cause catalyst degradation and
103 increase energy consumption [18]. Using an
104 external magnet, researchers have recently
105 paired magnetic nanoparticles with

106 photocatalytically active materials to improve
107 catalyst separation and recycling [19].
108 Therefore, the introduction of magnetic
109 materials such as Fe_3O_4 in $\text{Fe}_3\text{O}_4/\text{ZnO}/\text{CuO}$
110 nanocomposites simplifies the magnetic
111 separation. Nanocatalysts are beneficial for
112 academic and industrial research due to their
113 high reaction rates, perfect activation of
114 adsorbed compounds, ease of use, high
115 selectivity, recyclability, and eco-friendliness.
116 Because of their appealing features, nanometal
117 oxides have been utilized as solid catalysts in a
118 variety of organic processes [20].
119 In explaining the photocatalytic effect, it can be
120 said that in the absence of degradation matter,
121 hydrocarbons often decompose slowly.
122 Photocatalyst reduces the activation energy of
123 the decomposition process and therefore,
124 accelerates the reaction. As a result of the light
125 collision with photocatalytic materials,
126 electron holes create high oxidation and
127 resuscitation [21].
128 Nowadays, the use of ultrasonics in the
129 presence of a catalyst (sonocatalytic
130 decomposition) is an eco-friendly method for
131 removing dyes from wastewater. The influence
132 of ultrasonic waves is the heat produced by a
133 hole explosion, which converts water
134 molecules into hydroxyl radicals and reactive
135 hydrogen atoms. Both species can react with
136 organic dyes, which can lead to the breakdown
137 and elimination of different contaminants from
138 wastewater[22].
139 As a result, the simultaneous use of light and
140 ultrasonic radiation to analyze different colors
141 has been investigated [19-22].
142 In the current study, the impact of light and
143 ultrasound irradiation and the metal oxide
144 content has been investigated on the
145 photocatalytic activity of the $\text{Fe}_3\text{O}_4/\text{ZnO}/\text{CuO}$
146 nanocomposites. The optical and
147 morphological analysis proceeded with a
148 photocatalytic activity test in methylene blue
149 (MB) degradation from wastewater.
150
151 **2 EXPERIMENTAL PROCEDURES**
152
153 In this study Iron (II) sulfate heptahydrate
154 ($\text{FeSO}_4 \cdot 7\text{H}_2\text{O}$, 99%), copper sulfate
155 pentahydrate ($\text{CuSO}_4 \cdot 5\text{H}_2\text{O}$, 99%), zinc sulfate

156 heptahydrate ($\text{ZnSO}_4 \cdot 7\text{H}_2\text{O}$, 99%) and sodium
157 hydroxide (NaOH) (Merck Company) was
158 used as raw materials.

159 CuO and Fe_3O_4 nanoparticles were synthesized
160 using the sol-gel method. In this method, 0.025
161 mole of $\text{CuSO}_4 \cdot 5\text{H}_2\text{O}$ was dissolved in 100 mL
162 of deionized water with constant magnetic
163 stirring. Then 0.05 mole of NaOH was
164 dissolved in 150 mL of deionized water and
165 added to the solution in a droplet form to obtain
166 the appropriate pH. The solution was then
167 maintained at 80°C for 3 hours to form the gel.
168 After 4 hours, the black product was dissolved
169 using filter paper and dried at 80°C for 4 hours
170 in an oven to achieve Copper oxide
171 nanoparticles.

172 To obtain Fe_3O_4 nanoparticles, 0.027 mole of
173 $\text{FeSO}_4 \cdot 7\text{H}_2\text{O}$, dissolved in 100 mL of deionized
174 water and continuously stirred at room
175 temperature. To control the pH in 3, acetic acid
176 (CH_3COOH) and 30 mL of ethylene glycol
177 (EG), both of them in pure form, were added to
178 the solution. Then, 0.054 mole of NaOH was
179 dissolved in 150 mL of deionized water and
180 added dropwise to the mixture. The final
181 solution was stirred at 80°C for 3 h to form a
182 gel. The gel was dried at 80°C for 4 h.

183 To synthesize the $\text{Fe}_3\text{O}_4/\text{ZnO}/\text{CuO}$
184 nanocomposite, 0.0125 mole of $\text{ZnSO}_4 \cdot 7\text{H}_2\text{O}$
185 was dissolved in 30 mL of distilled water with
186 magnetic stirring. Then, 0.025 mole of NaOH
187 in 65 mL of deionized water was added to the
188 solution in droplets to reach the appropriate
189 PH, which was then stirred and heated at 80°C .
190 The previously synthesized Fe_3O_4 and CuO
191 nanoparticles were dispersed in 30 mL of
192 ethanol (99.7%) and then added to the initial
193 solution. The resulting mixture was
194 continuously stirred at 80°C for 2 hours.
195 Finally, ZnO was formed in situ on the surface
196 of the pre-formed Fe_3O_4 and CuO. At the end
197 the product was isolated using filter paper and
198 washed several times with distilled water and
199 ethanol to remove impurities. The final product
200 was left at room temperature overnight and
201 dried at 100°C for 1 hour. Nanocomposite
202 $\text{Fe}_3\text{O}_4/\text{ZnO}/\text{CuO}$ with the molar ratios of
203 (1:1:0.3, 1:1:0.5, 1:1:1, 1:1:3) was prepared by
204 changing the concentrations of the precursor
205 solutions and evaluated.

206 X-ray diffraction peaks were measured by an
207 XRD analyzer (Siemens D5000 X-ray
208 diffractometer). The analysis was conducted
209 under the conditions of Cu- α radiation
210 ($\lambda=1.54178\text{\AA}$), a scanning rate of $20^\circ/\text{min}$, a 2θ
211 range of $20-80^\circ$, and operating conditions of 30
212 kV and 40 mA. Also, Crystallite size is
213 estimated by Scherer's equation (Eq.1) [23]:
214 $D=0.9\lambda/\beta\text{Cos}\Theta$ (Eq. 1)

215 where D is the size of the crystals in
216 nanometers, β is the peak width at half the
217 maximum intensity in radians in radian, λ is the
218 x-ray wavelength in nanometers, and Θ is the
219 Bragg angle corresponding to the diffraction
220 peak.

221 SEM (Stereo Scan 360) was conducted to
222 verify the morphology of the obtained
223 nanoparticles. Elemental analysis of the
224 samples was performed using X-ray diffraction
225 spectroscopy (EDX). A dot map was used to
226 determine the distribution of the elements in the
227 nanocomposite. To investigate particle size
228 distribution from DLS, Nanotracc Wave of
229 Micro trac Co. was used and to determine the
230 adsorption edge and band gap of synthesized
231 zinc oxide and prepared nanocomposites, DRS
232 spectroscopic analysis was performed. The
233 absorption wavelength was obtained by
234 extrapolating the linear part of the absorption
235 intensity curve in terms of wavelength.

236 Eq. 2 was used to calculate the band gap [24]:
237 $E_g = hc / \lambda_g$ (Eq. 2)

238 In this respect, E_g is the band gap in electron
239 volts, h is the Planck constant equals
240 4.13567×10^{-15} eV, c is the light speed equals
241 299792458 m / s and λ_g is the absorption
242 wavelength.

243 The effectiveness of the photocatalysts was
244 tested by measuring their ability to break down
245 methylene blue (MB) in 100 mL beakers. In
246 this test, the UV-C Philips 9W lamp was used
247 as UV light and the 120-watt metal halide lamp
248 was used as a visible light source. A
249 photocatalytic test equipment was mounted and
250 sealed in a dark chamber to prevent the loss of
251 radiation. For the determination of
252 photocatalytic activity, 0.05 g of the
253 nanocomposite samples was dispersed in 100
254 ml of MB solution with a concentration of
255 0.005 g / l using a magnetic stirrer.
256 Before illumination, the reaction mixture was

257 kept in dark conditions for 20 minutes to
258 establish adsorption-desorption equilibrium.
259 After collecting the initial sample, the
260 photocatalytic reaction was initiated by
261 activating the light source. Subsequent samples
262 were collected at 20-minute intervals
263 (specifically at 20, 40, 60, 80, 100, and 120
264 minutes), and each sample underwent UV-Vis
265 spectroscopic analysis. The concentration of
266 Methylene Blue (MB) was determined by
267 measuring the UV-Vis absorbance at its
268 characteristic peak wavelength of 665 nm. A
269 calibration curve was created and used to
270 convert the measured absorbance values into
271 actual dye concentrations. The degradation rate
272 was then determined using the following
273 equation [25]:

$$275 \quad (I_0 - I_t) / I_0 \times 100 = (C_0 - C_t) / C_0 \times 100 \quad (\text{Eq. 3})$$

276
277 Where C represents the concentration of
278 Methylene Blue (MB) at any given time during
279 the reaction, while C₀ is the initial MB
280 concentration after reaching adsorption-
281 desorption equilibrium, similarly, A represents
282 the absorbance value measured at any point
283 during the reaction, and A₀ is the initial
284 absorbance value recorded at equilibrium.
285 To evaluate how ultrasonic treatment affects
286 photocatalytic activity, Fe₃O₄/ZnO/CuO
287 nanocomposites (0.05 g) with varying molar
288 ratios were dispersed in Methylene Blue
289 solution (100 mL, 0.005 g/L) using
290 ultrasonication and subjected to visible light
291 irradiation for intervals of 20, 40, 60, 80, 100
292 and 120 minutes.

294 3 Results and Discussions

295
296 The XRD patterns shown in Fig. 1 display the
297 diffraction patterns of Fe₃O₄/ZnO/CuO
298 nanocomposites that were synthesized in
299 different molar ratios of CuO. The patterns
300 exhibit characteristic diffraction peaks
301 corresponding to cubic spinel Fe₃O₄,
302 monoclinic CuO, and hexagonal wurtzite ZnO
303 structures. The absence of any impurities or
304 secondary phases in the patterns demonstrates
305 that the Fe₃O₄/ZnO/CuO nanocomposites were
306 synthesized successfully. All XRD peaks
307 corresponding to [101] Planes related to

308 hexagonal ZnO structure (2θ =32.5), [200]
309 planes related to CuO monoclinic structure (2θ
310 =39.5) and [311] planes for cubic spinel
311 structure Fe₃O₄ (2θ =35.5) have the highest
312 growth rates. Furthermore, analysis of the XRD
313 patterns for Fe₃O₄/ZnO/CuO nanocomposites
314 with varying molar ratios reveals a clear trend:
315 as the molar ratio of CuO to ZnO increases,
316 there is a corresponding increase in the
317 intensity of CuO diffraction peaks, while
318 simultaneously showing a decrease in the
319 intensity of both ZnO and Fe₃O₄ diffraction
320 peaks. Changes in the intensity of the pattern
321 revealed the increase of CuO content within
322 the nanocomposite structure.

323 In all XRD diagrams, considering the peak
324 positions, it can be seen that ZnO does not form
325 a solid solution with CuO and Fe₃O₄, and the
326 Fe₃O₄/ZnO/CuO nanocomposite is considered
327 as a nanocomposite powder of ZnO, Fe₃O₄ and
328 CuO crystals.

329 Fig. 2 shows the XRD pattern of
330 Fe₃O₄/ZnO/CuO nanocomposite with molar
331 ratios of 1:1:0.3, 1:1:0.5, 1:1:1, and 1:1:3 for
332 a,b,c, and d images, respectively. According to
333 reference data, 01-075-0033 demonstrated
334 Fe₃O₄ in the cubic phase, 0254-041-00
335 determined the hexagonal crystalline phase of
336 ZnO, and 0704-076-01 demonstrated CuO with
337 a monoclinic crystalline structure.

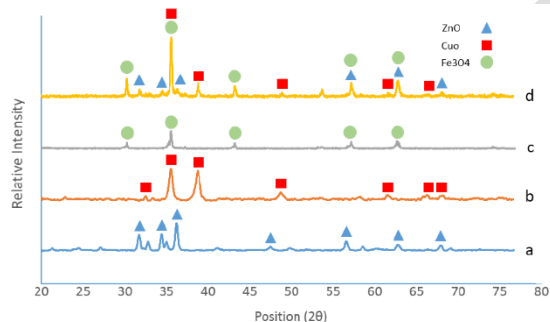
338 In Table. 1, the particle size of Fe₃O₄, ZnO,
339 CuO, and Fe₃O₄/ZnO/CuO nanocomposites
340 with molar ratios of 1:1:0.3, 1:1:0.5, 1: 1: 1 and
341 1: 1: 3 estimated by Scherrer's equation. By
342 comparing the size of Fe₃O₄, ZnO, and CuO
343 particles in Fe₃O₄/ZnO/CuO nanocomposites
344 with different molar ratios, it is observed that
345 the presence of CuO inhibits the growth of
346 particles and reduces the size of ZnO and Fe₃O₄
347 particles. In conclusion, CuO nanoparticles
348 inhibit the growth of ZnO crystallites. It was
349 evidenced by the significant reduction in ZnO
350 crystallite size in the presence of CuO. In
351 contrast, Fe₃O₄ crystallite size shows a smaller

352 decrease, indicating that CuO has a less
 353 pronounced effect on the growth of Fe₃O₄
 354 crystallites. The crystallite size of CuO varies
 355 depending on its concentration in the
 356 composites, highlighting its role in controlling
 357 crystallite growth in nanocomposites.

358 **Table 1.** crystallite size of ZnO, CuO, and Fe₃O₄ in
 359 Fe₃O₄/ZnO/CuO nanocomposite

samples	ZnO crystallite size (nm)	CuO crystallite size (nm)	Fe ₃ O ₄ crystallite size (nm)
Fe ₃ O ₄	-	-	44.5
CuO	-	19.31	-
ZnO	22.92	-	-
Fe ₃ O ₄ /ZnO/CuO(1:1:0.3)	19.21	20.15	44.01
Fe ₃ O ₄ /ZnO/CuO (1:1:0.5)	20.18	16.15	42.23
Fe ₃ O ₄ /ZnO/CuO (1:1:1)	19.65	18.62	41.15
Fe ₃ O ₄ /ZnO/CuO (1:1:3)	17.15	21.48	40.15

361

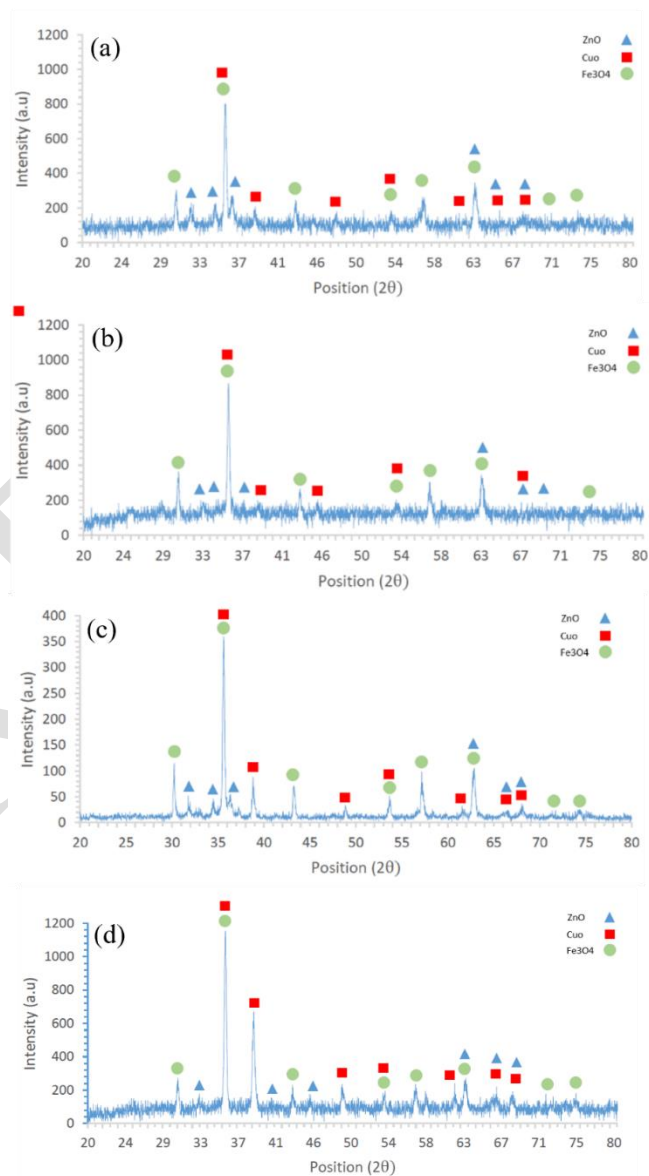


362

363 **Fig. 1.** XRD patterns of synthesized
 364 Fe₃O₄/ZnO/CuO nanocomposite: (a) ZnO, (b)
 365 CuO, (c) Fe₃O₄, (d) Fe₃O₄/ZnO/CuO
 366 nanocomposite.

368 Particle morphology of nanocomposites was
 369 investigated by scanning electron microscopy
 370 (SEM). Fig. 3 illustrates an SEM image of a
 371 Fe₃O₄/ZnO/CuO nanocomposite with a molar
 372 ratio of 1:1:0.5. As shown in Fig.3, the
 373 Fe₃O₄/ZnO/CuO nanocomposite is
 374 cauliflower-shaped. To compare the results, the
 375 size distribution of the conventional and
 376 synthesized catalysts was considered using
 377 ImageJ software. The analysis revealed that the
 378 synthesized samples exhibited relatively small
 379 average particle dimensions. This size
 380 distribution indicates the successful formation

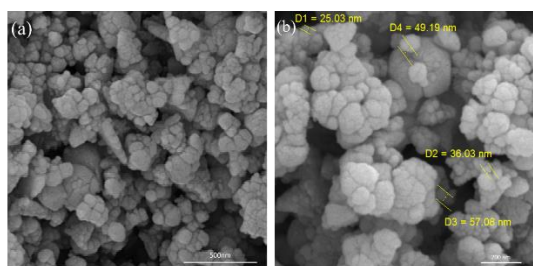
381 of nanostructured materials. Similar
 382 Fe₃O₄/ZnO/CuO morphologies have been
 383 reported in previous studies[20].
 384



385 **Fig. 2.** XRD patterns of synthesized
 386 Fe₃O₄/ZnO/CuO nanocomposite: (a)
 387 Fe₃O₄/ZnO/CuO (1:1:0.3),
 388 (b) Fe₃O₄/ZnO/CuO(1:1:0.5), (c) Fe₃O₄/ZnO/CuO
 389 (1:1:1) and (d) Fe₃O₄/ZnO/CuO(1:1:3).

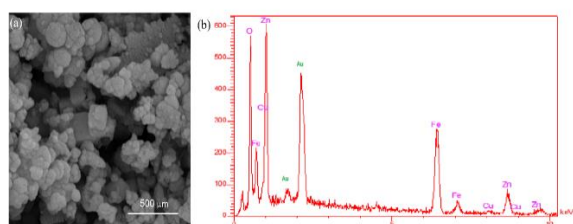
391
 392 Above all, the numerous pores of different
 393 sizes within the 3D microstructure act as
 394 transport pathways for small molecules. This
 395 morphology and porosity provide a larger
 396 surface area for dye adsorption and catalytic
 397 reactions. The reduction in particle dimensions

398 enhances the generation of electron-hole pairs
 399 when exposed to light, resulting in more
 400 effective degradation of contaminants during
 401 performance testing.
 402



403
 404 **Fig. 3.** SEM image of synthesized Fe₃O₄/ZnO/CuO
 405 nanocomposite, (a) SEM Mag 70kx
 406 (b) SEM Mag 100kx Particle Size Distribution
 407

408 EDX analysis aims to define the dispersion of
 409 the elements on the surface of the catalyst. As
 410 shown in Fig. 4, the characteristic peaks of the
 411 elements of oxygen, iron, copper, and zinc
 412 indicate the presence of these elements in the
 413 nanocomposite structure. It should be noted
 414 that the samples had no impurities. The peak in
 415 the range of 1.8 and 2.2 keV is related to the
 416 gold element, covered on the nanocomposite in
 417 SEM analysis, to provide conductivity in the
 418 sample. Also in Table 2, the weight percentage
 419 and atomic percentage of the elements are
 420 specified, which proves the proper synthesis of
 421 the samples.



422
 423 **Fig. 4.** EDX analysis of synthesized
 424 Fe₃O₄/ZnO/CuO nanocomposite: (a) SEM image
 425 of the area selected for EDX analysis, (b) EDX
 426 results in Fe₃O₄/ZnO/CuO nanocomposite (1:1:0.5)
 427

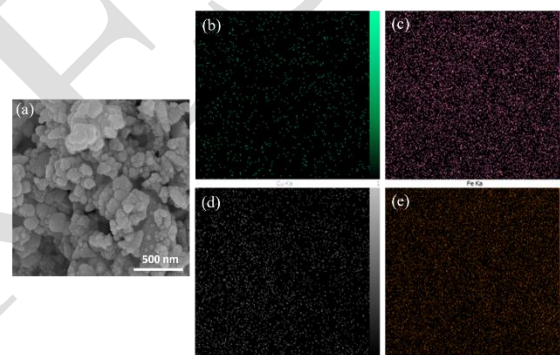
428
 429
 430 **Table 2.** Comparative amount of elements in the
 431 structure of Fe₃O₄/ZnO/CuO nanocomposite
 432 (1:1:0.5)

samples	Weight percentage (% W)	Atomic percentage (% A)
O K _α	28.77	60.03
Cu K _α	1.72	0.9
Zn K _α	28.38	14.49
Fe K _α	41.12	24.57

433
 434

435 To investigate the distribution of elements in
 436 the photocatalyst structure, dot Map analysis
 437 was prepared from Fe₃O₄/ZnO/CuO
 438 nanocomposite (1:1:0.5) as shown in Fig. 5.
 439 The elemental distribution analysis of the
 440 photocatalyst structure was conducted on the
 441 selected region shown in Fig. 5a. Images 5b,
 442 5c, 5d, and 5e show the distribution of copper,
 443 iron, zinc, and oxygen, respectively. Moreover,
 444 the elements are homogeneously distributed in
 445 the structure.

446



447
 448 **Fig. 5.** Dot map analysis of synthesized
 449 Fe₃O₄/ZnO/CuO nanocomposite: (a) Selected area
 450 for dot map analysis, (b) Cu, (c) Fe, (d) Zn, (e) O
 451

452 In this study, the photocatalytic performance of
 453 Fe₃O₄/ZnO/CuO nanocomposites was
 454 investigated by analyzing the relationship
 455 between band gap and varying molar ratios of
 456 the components. The photocatalytic
 457 degradation efficiency of pollutants is
 458 primarily determined by the band gap, which
 459 serves as the critical parameter in the process.
 460 For this purpose, the absorption spectrum of
 461 nanocomposites was measured by a UV-visible
 462 device, and the results are shown in Fig. 6(a).
 463 The bandgap energies of the samples were
 464 determined using Tauc's plots by extrapolating
 465 the linear part of plots to the hv axis as shown
 466 in Fig. 6 (b).

467 ZnO nanoparticles exhibit strong absorption in
 468 the wavelength range of 200-400 nm, and the

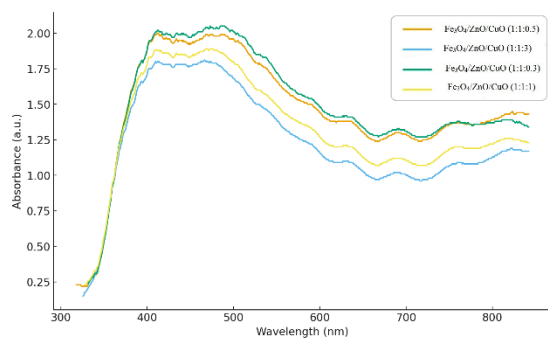
469 absorption edge of the samples shifts to 372 nm
 470 with increasing copper oxide content in the
 471 visible light region. Coupling zinc oxide with
 472 copper oxide leads to a narrowing of the band
 473 gap. This reduction in the band gap occurs
 474 because the addition of copper oxide to the
 475 nanocomposite introduces an intermediate
 476 energy band at the bottom of the conduction
 477 band of zinc oxide. This interaction decreases
 478 the energy difference between the valence band
 479 and the conduction band of zinc oxide, thereby
 480 reducing the overall band gap energy.

481 According to the literature, ZnO nanoparticles
 482 are n-type semiconductors, and the
 483 semiconductor CuO nanoparticles are p-type.
 484 In this study, the photocatalytic performance
 485 was enhanced by creating a heterojunction
 486 between n-type and p-type semiconductors,
 487 while simultaneously studying how this
 488 junction influences the optical characteristics.
 489 In Table 3, the absorption wavelength and
 490 energy of the band gap region for each sample
 491 are calculated using the following equation:

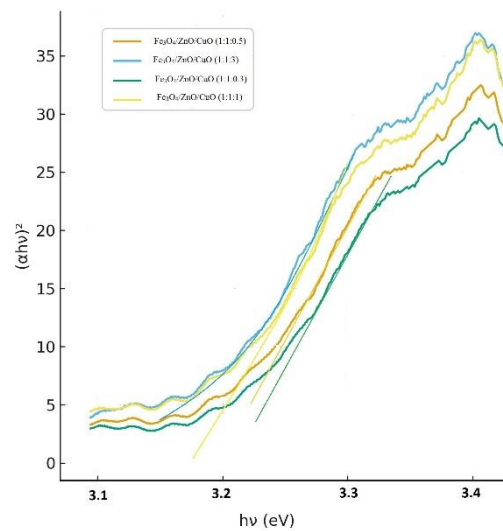
$$492 (\alpha h\nu)^2 = A(h\nu - E_g) \quad (Eq.4)$$

493 where α is the absorption coefficient, h is
 494 Planck's constant, ν is the photon frequency,
 495 E_g is the optical band gap, and A and n are
 496 constants. For the direct bandgap
 497 semiconductor, $n = 2$, and for the indirect
 498 transition bandgap, $n = 1/2$. We assumed $n = 2$ for
 499 our samples.

500
 501
 502



a)



b)

504
 505 **Fig. 6.** Bandgap analysis curves of Fe₃O₄/ZnO/CuO
 506 nanocomposite: a) UV-VIS Absorption Spectra, b)
 507 Tauc's plots graphs (n=2)

508
 509
 510
 511 **Table 3.** Wavelength values of the absorption edge
 512 and the energy of the band gap of ZnO and
 513 Fe₃O₄/ZnO/CuO nanocomposites

Samples	Wavelength of absorption edge (nm)	Energy of the band gap (eV)
ZnO	382.16	3.24
Fe ₃ O ₄ /ZnO/CuO (1:1:0.3)	384.1	3.22
Fe ₃ O ₄ /ZnO/CuO (1:1:0.5)	386.31	3.20
Fe ₃ O ₄ /ZnO/CuO (1:1:1)	389.26	3.18
Fe ₃ O ₄ /ZnO/CuO (1:1:3)	398.54	3.11

514
 515

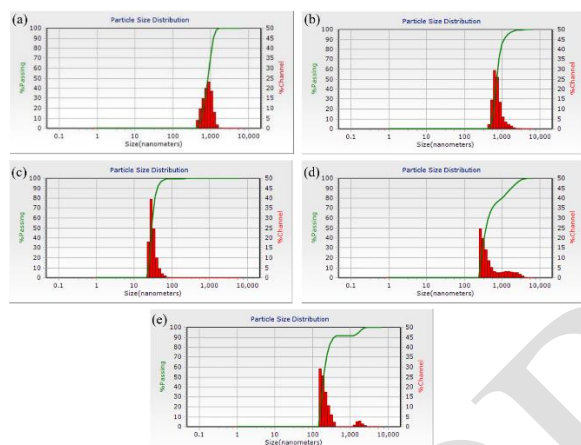
516 DLS analysis was performed to investigate
 517 particle size distribution. Fig. 7 illustrates the
 518 range of particle size distribution in the ZnO,
 519 Fe₃O₄/ZnO/CuO(1:1:0.3),
 520 Fe₃O₄/ZnO/CuO(1:1:0.5),
 521 Fe₃O₄/ZnO/CuO(1:1:1) and
 522 Fe₃O₄/ZnO/CuO(1:1:3) samples are 486-1944,
 523 486-6540, 25-409, 289-6540, 171.9-6540 nm,
 524 respectively.

525 On the other hand, the highest number of
 526 particles in the ZnO, Fe₃O₄/ZnO/CuO(1:1:0.3),
 527 Fe₃O₄/ZnO/CuO (1:1:0.5), Fe₃O₄/ZnO/CuO
 528 (1:1:1), and Fe₃O₄/ZnO/CuO (1:1:3) samples
 529 are 972, 687, 30.04, 289, and 171.9 nm,
 530 respectively. DLS measures the hydrodynamic
 531 diameter of particles (or agglomerates) in a
 532 solution, which is typically much larger than

503

533 the primary particle size seen in SEM or the
 534 crystallite size from XRD. The results show
 535 that increasing the percentages of CuO in the
 536 Fe₃O₄/ZnO/CuO nanocomposite does not have
 537 a steady effect on particle size. In general,
 538 although the particle size in the nanocomposite
 539 decreased compared to the particle size in pure
 540 ZnO samples but also the DLS data also
 541 indicate severe agglomeration of the primary
 542 nanoparticles in suspension, which is a critical
 543 factor for photocatalytic performance as it
 544 affects the active surface area.

545



546

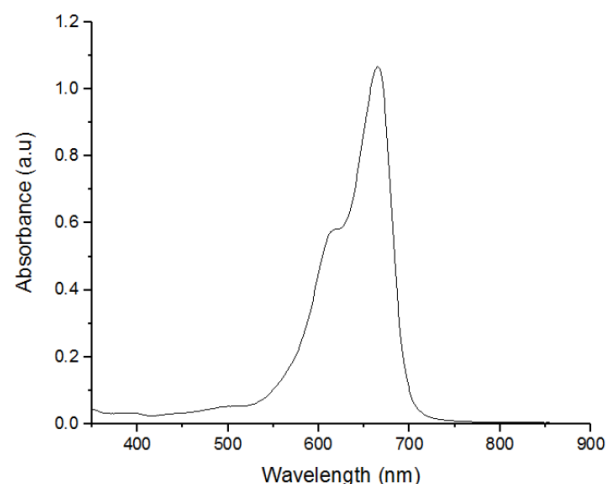
547 **Fig. 7.** DLS Analysis Results of Fe₃O₄/ZnO/CuO
 548 nanocomposites, (a) ZnO, (b) Fe₃O₄/ZnO/CuO
 549 (1:1:0.3),
 550 (c) Fe₃O₄/ZnO/CuO (1:1:0.5), (d) Fe₃O₄/ZnO/CuO
 551 (1:1:1), (e) Fe₃O₄/ZnO/CuO (1:1:3)

552

553 To investigate the various factors that affect the
 554 photocatalytic properties, the Fe₃O₄/ZnO/CuO
 555 nanocomposites with different molar ratios in
 556 MB solution were individually irradiated with
 557 UV and visible waves at 20-40-60-80-100-120
 558 minutes. Fig. 8 shows the absorption spectrum
 559 of MB before photocatalytic activity. The
 560 absorption rate of methylene blue is
 561 approximately 1.067 at 665 nm. The reduction
 562 of this amount in the presence of
 563 Fe₃O₄/ZnO/CuO nanocomposite and ZnO
 564 samples under visible and UV radiation reflects
 565 the color of this industrial dye. It demonstrates
 566 the ability of this nanocomposite to treat
 567 industrial wastewater.

568

569



570

571

572

Fig. 8. Absorption spectrum of methylene blue
 before photocatalytic activity.

573

574

575

576

577

578

579

580

581

582

583

584

585

586

587

588

589

590

591

592

593

594

595

596

597

598

599

600

601

602

603

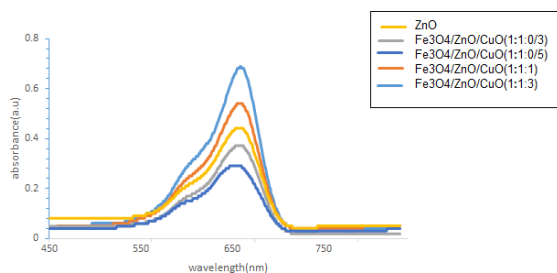
604

605

Fig. 9 shows the results of the photocatalytic
 activity under UV irradiation for over 120
 minutes. The methylene blue absorption peak,
 which had an initial concentration of 0.005 g/
 L, decreased after 120 min in each sample. The
 amount of methylene blue dye removal by the
 Fe₃O₄/ZnO/CuO samples with a molar ratio of
 1:1:0.5 is higher than in other samples. The
 photocatalytic activity of samples is
 58.76%, 65.32%, 72.82%, 49.39%, and 35.33%
 for ZnO, Fe₃O₄/ZnO/CuO with the molar ratio
 of 1:1:0.3, 1:1:0.5, 1:1:1, 1:1:3 respectively,
 which were calculated using the formula.

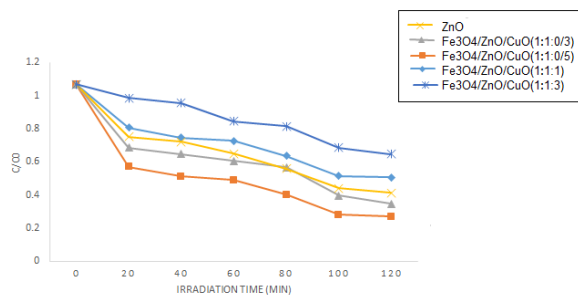
Fig. 10 illustrates a comparative diagram of the
 photocatalytic performance of Fe₃O₄/ZnO/CuO
 nanocomposites with different amounts of CuO
 under UV irradiation for 20 to 120 minutes.
 Under UV irradiation, Fe₃O₄/ZnO/CuO
 nanocomposites with 1:1:1 and 1:1:3 molar
 ratios have lower photocatalytic activity than
 pure ZnO. The shift of the absorption edge
 towards the visible spectrum and the reduction
 in band gap of the nanocomposites can be
 attributed to the incorporation of CuO. Due to
 the differences between the UV wave energy
 with the amount of energy which was needed
 to transfer electrons from the valence band to
 the conduction band in Fe₃O₄/ZnO/CuO
 nanocomposites, and the low efficiency of
 electron-cavity generation compared to ZnO,
 the above nanocomposites exhibit less
 photocatalytic activity.

606



607
608 **Fig. 9.** Photocatalytic activity of Fe₃O₄/ZnO/CuO
609 nanocomposites under UV radiation.

610

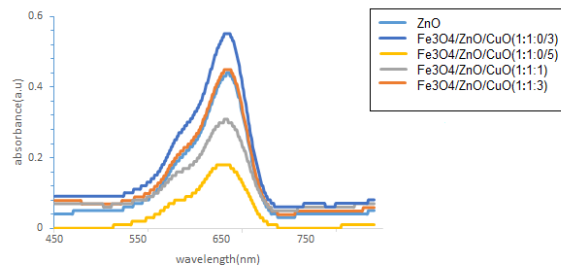


611
612 **Fig. 10.** Comparative diagram of Fe₃O₄/ZnO/CuO
613 nanocomposites' photocatalytic efficiency under
614 UV radiation.

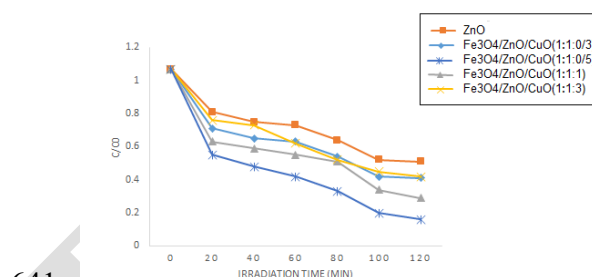
615

616 Fig. 11 shows the results of the photocatalytic
617 activity under visible irradiation for over 120
618 minutes. The Fe₃O₄/ZnO/CuO composite with
619 a 1:1:0.5 molar ratio demonstrated superior
620 methylene blue dye removal compared to other
621 samples. The photocatalytic degradation
622 efficiencies were measured at 48.45% for pure
623 ZnO, and for Fe₃O₄/ZnO/CuO composites:
624 62.27% at 1:1:0.3 ratio, 88.7% at 1:1:0.5 ratio,
625 77.94% at 1:1:1 ratio, and 57.82% at 1:1:3
626 ratio. Fig. 12 shows a comparative diagram of
627 the photocatalytic activity of Fe₃O₄/ZnO/CuO
628 nanocomposites with different amounts of CuO
629 under visible irradiation for 20 to 120 minutes.
630 The Fe₃O₄/ZnO/CuO nanocomposite with a 1:
631 1: 0.5 molar ratio exhibits the best
632 photocatalytic activity. However, the
633 photocatalytic activity of the samples improved
634 concerning pure ZnO, indicating the higher
635 photocatalytic activity of Fe₃O₄/ZnO/CuO
636 nanocomposites in the visible light range.

637



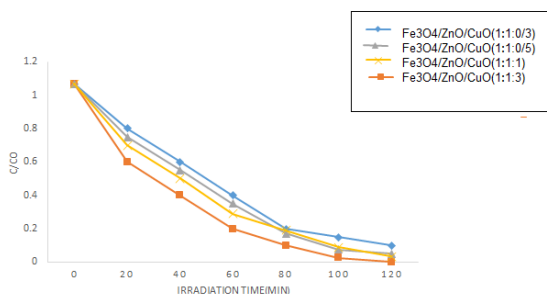
638
639 **Fig. 11.** photocatalytic activity of Fe₃O₄/ZnO/CuO
640 nanocomposites under visible radiation.



641
642 **Fig. 12.** Comparative diagram of photocatalytic
643 efficiency of Fe₃O₄/ZnO/CuO nanocomposites
644 under visible radiation.

645

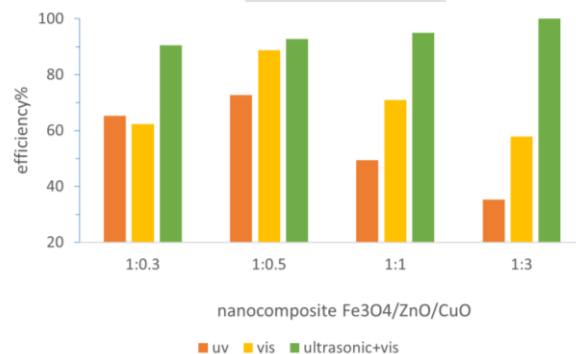
646 To investigate the influence of ultrasound on
647 the photocatalytic activity of the
648 Fe₃O₄/ZnO/CuO nanocomposites with
649 different molar ratios, the nanocomposites
650 were irradiated with ultrasonic and visible light
651 for 20-120 minutes in a methylene blue
652 solution, and their photocatalytic activity was
653 measured. Fig. 13 illustrates this. The results
654 showed that the Fe₃O₄/ZnO/CuO
655 nanocomposites with the molar ratio of 1:1:3
656 have the highest photocatalytic activity under
657 ultrasound and visible light irradiation. The
658 enhanced performance can be attributed to
659 CuO's appropriate band gap characteristics.
660 Under ultrasonic conditions, CuO showed
661 higher activation compared to ZnO, and
662 increasing the CuO content led to improved
663 photocatalytic activity. As illustrated in Fig. 13,
664 complete photocatalytic degradation (100%
665 efficiency) was achieved after 120 minutes of
666 treatment.



667
668 **Fig. 13.** Comparative diagram of photocatalytic
669 efficiency of Fe₃O₄/ZnO/CuO nanocomposites
670 under visible and ultrasound radiation.
671

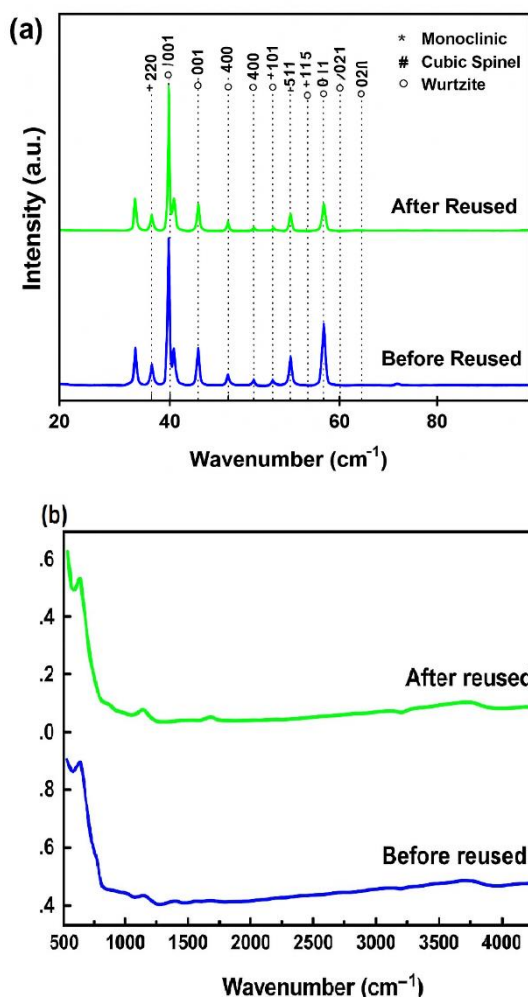
672 The Fe₃O₄/ZnO/CuO nanocomposites with
673 different molar ratios were investigated under
674 UV, visible, and ultrasonic waves, and their
675 comparative results are shown in Fig. 14.
676 Enhancing photocatalytic activity of the
677 nanocomposite under visible light and
678 ultrasonic by increasing CuO content is mainly
679 attributed to the narrow band gap of CuO,
680 which enables strong visible-light absorption
681 and promotes efficient charge separation
682 through the formation of the n-p
683 heterojunction. In this procedure, CuO acts as
684 an effective electron trap, repressing
685 recombination and enhancing the generation of
686 reactive species. Under ultrasonic-visible light,
687 the highest efficiency was observed, which can
688 be driven by two reasons. Firstly, Ultrasonic
689 increases the production of active radicals for
690 photocatalytic activity, and also improves the
691 organic transfer of color between the catalyst
692 surface. secondly, the de-agglomeration of
693 photocatalysis particles by ultrasonication
694 leads to an increase in the specific surface area.
695 The ultrasonic process operates through
696 cavitation that forms holes, leading to elevated

697 temperature and pressure conditions in the
698 reaction medium. This process involves the
699 formation, gradual growth, and eventual
700 bursting of a series of bubbles by sonication.
701 Under such conditions, hot spots are created
702 that can convert water molecules into active
703 hydroxyl radicals and hydrogen peroxide, and
704 these active radicals destroy toxic compounds.



705
706 **Fig. 14.** Comparative diagram of photocatalytic
707 efficiency of Fe₃O₄/ZnO/CuO nanocomposites
708 under UV, visible, and ultrasonic radiation.
709

710 Based on other related research, stability of
711 the catalysts under light and ultrasonic
712 irradiation was evaluated by the same batch of
713 nanocomposites for four cycles, with the same
714 amount of fresh MB solutions added after each
715 run. The results in Fig. 15 show that the
716 catalysts exhibit good stability and magnetic
717 recyclability from the treated solutions after
718 successive degradation reactions.
719 The XRD and FTIR measurements were also
720 performed on the catalysts after multiple
721 cycles, and compared with the results obtained
722 before the reaction. In Fig. 15(a), all XRD peaks
723 corresponding to cubic spinel, hexagonal
724 wurtzite, and monoclinic structures remained at
725 the same values after four cycles. So, there is
726 no change in the crystalline structure.
727 The same conclusion is drawn from the IR
728 absorption measurements because the IR peaks
729 of the functional groups remain unchanged
730 after photocatalytic degradation, Fig. 15(b)
731 [30].



732

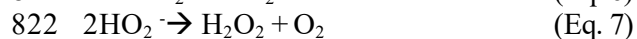
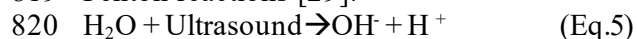
733 **Fig. 15.** a) XRD patterns of $\text{Fe}_3\text{O}_4/\text{ZnO}/\text{CuO}$
 734 nanocomposites after and before reused, b) IR
 735 peaks of $\text{Fe}_3\text{O}_4/\text{ZnO}/\text{CuO}$ nanocomposites after
 736 and before reused [30]

737

738 Various factors such as the generation, trapping
 739 of electrons, charge carrier recombination, the
 740 average size of the crystals, and the energy of
 741 the band gap, are important factors that we can
 742 propose the mechanism of the photocatalyst.
 743 The varying molar proportions of CuO in the
 744 samples significantly influence the
 745 photocatalytic mechanism. Research has
 746 shown that a larger specific surface area creates
 747 more active surface sites, which reduces the
 748 interfacial charge carrier transfer resistance and
 749 enhances photocatalytic performance. The
 750 nanocomposites show different patterns of
 751 photocatalytic performance when exposed to
 752 visible light versus UV radiation.

753 The diffuse reflectance spectroscopy analysis
 754 revealed that ZnO has a band gap of 3.24 eV,
 755 while CuO exhibits a band gap of 1.54 eV[30].
 756 As an n-type semiconductor, ZnO's electrons in
 757 the valence band become excited and move to
 758 the conduction band when exposed to UV
 759 radiation, which is possible due to its specific
 760 band gap energy. In contrast, CuO, being a p-
 761 type semiconductor, can achieve electron
 762 transfer from the valence to the conduction
 763 band through visible light exposure. The
 764 complementary band gap energies of ZnO,
 765 CuO, and Fe_3O_4 can enhance electron transfer
 766 between these materials. When exposed to
 767 visible light, CuO generates electron-hole pairs
 768 because of its favorable band gap.
 769 Additionally, electrons from ZnO's valence
 770 band, which possess lower energy compared to
 771 its conduction band, can move into structural
 772 defects like oxygen vacancies. When CuO's
 773 excited electrons migrate to ZnO's conduction
 774 band, they can interact with Fe^{3+} to form Fe^{2+}
 775 ions. These unstable Fe^{2+} ions then react with
 776 oxygen molecules to generate superoxide
 777 radicals. Simultaneously, holes created in
 778 ZnO's valence band can either transfer to CuO's
 779 valence band or interact with water molecules
 780 to create OH^\cdot . Additionally, holes in CuO can
 781 also generate hydroxyl radicals through water
 782 interaction. Under UV light, the capture of
 783 electrons by Fe^{3+} ions enhances the probability
 784 of hole-mediated hydroxyl radical formation,
 785 which then breaks down organic pollutants.
 786 During this process, electrons from ZnO's
 787 valence band are exclusively excited to its
 788 conduction band, creating holes in the valence
 789 band. These excited electrons are captured by
 790 Fe^{3+} ions, forming Fe^{2+} ions that produce
 791 superoxide radicals. Concurrently, the
 792 photogenerated holes react with water
 793 molecules to form OH^\cdot radicals, which are the
 794 key agents in decomposing methylene blue
 795 during the catalytic reaction [26-28].
 796 The mechanism behind MB degradation using
 797 ultrasonic treatment has been verified. When
 798 ultrasonic waves are applied, they induce
 799 acoustic cavitation, generating extreme
 800 conditions of temperature (5000 K) and
 801 pressure (1000 atm). This process produces
 802 light across a broad wavelength spectrum
 803 (sonoluminescence), activating both ZnO and

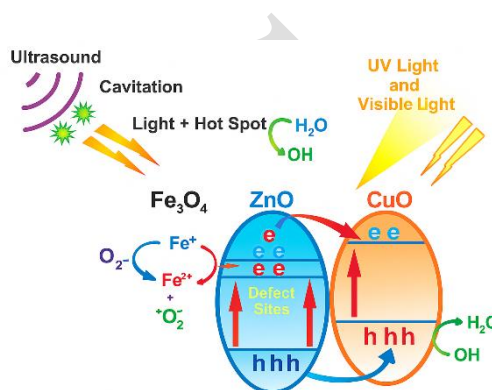
804 CuO semiconductors and forming electron-
 805 hole pairs [28]. These electron-hole pairs
 806 contribute to MB degradation through the same
 807 mechanisms observed in photocatalysis. When
 808 exposed to both visible light and ultrasound,
 809 CuO shows enhanced activation due to its
 810 suitable band gap energy. This explains why
 811 the nanocomposite containing the highest
 812 proportion of CuO (Fe₃O₄/ZnO/CuO in a 1:1:3
 813 molar ratio) demonstrates superior
 814 photosonocatalytic performance under visible
 815 light conditions. Moreover, the extreme
 816 temperature and pressure conditions created by
 817 ultrasound in aqueous environments promote
 818 the direct formation of OH⁻ radicals through
 819 Fenton reactions [29]:



824 According to Yuan and colleagues' research
 825 [30], the H₂O₂ produced (as shown in Eq. 7) can
 826 interact with Fe²⁺ to generate OH⁻ radicals and
 827 Fe³⁺ ions. The increased production of OH
 828 radicals through various pathways under
 829 ultrasonic irradiation results in improved
 830 degradation efficiency.

831 The reason that the ternary nanocomposite with
 832 the ratio of 1:1:0.5 is optimal under visible
 833 light, while 1:1:3 is best under sonolysis, is
 834 attributed to the narrow band gap of CuO,
 835 which enables strong visible-light absorption
 836 and promotes efficient charge separation
 837 through the formation of the n-p
 838 heterojunction. In this procedure, CuO acts as
 839 an effective electron trap, repressing
 840 recombination and enhancing the generation of
 841 reactive species. In contrast, under UV
 842 irradiation, increasing the ratio of CuO in the
 843 nanocomposite reduces the photocatalytic
 844 performance because CuO does not absorb UV
 845 efficiently and partially covers the surface of
 846 the primary semiconductor (reducing the

847 specific interface areas). Also, agglomeration
 848 occurs by increasing CuO content, which limits
 849 the UV absorption. Moreover, extra CuO can
 850 behave as recombination centers, accelerating
 851 electron-hole recombination and lowering the
 852 overall photocatalytic activity.



853
 854 **Fig. 16.** Schematic of the photocatalytic
 855 mechanism of Fe₃O₄ / ZnO / CuO nanocomposites

856 4 Conclusions

857 In conclusion, the Fe₃O₄/ZnO/CuO
 858 nanocomposites were successfully produced
 859 using the sol-gel synthesis technique. The
 860 degradation of methylene blue was examined
 861 under both light and ultrasonic irradiation to
 862 analyse the photocatalytic activity. Results
 863 revealed that ultrasonic treatment played a
 864 crucial role and significantly improved the
 865 photocatalytic performance of the
 866 nanocomposite materials. The optimal
 867 composition of the photocatalyst
 868 nanocomposite material was investigated
 869 through structural characterization using
 870 various techniques. SEM images shown that
 871 the nanocomposite exhibited a cauliflower-like
 872 structure with particle size distribution ranging
 873 from 25.3 to 57.08 nm, as measured by ImageJ
 874 software. EDX analysis also confirmed
 875 improved dispersion of the samples.
 876 Additionally, dot mapping of the
 877 nanocomposite structure indicated that the
 878 elements were uniformly distributed
 879 throughout the material. Dynamic Light
 880 Scattering (DLS) results showed that
 881 increasing the copper oxide content in the
 882 Fe₃O₄/ZnO/CuO nanocomposite led to a
 883 reduction in particle size distribution.

884 Moreover, the addition of CuO decreased the
 885 band gap energy, shifting light absorption
 886 toward the visible region. The photocatalytic
 887 performance revealed 100% degradation of
 888 MB for Fe₃O₄/ZnO/CuO nanocomposite at a
 889 1:1:3 molar ratio under ultrasound and visible
 890 light after 120 minutes. Additionally, the use of
 891 an external magnet allowed for easy separation
 892 and recovery of the nanocomposite from the
 893 solution after the reaction. These findings
 894 highlight the effectiveness of the ternary
 895 Fe₃O₄/ZnO/CuO nanocomposite catalyst in
 896 removing organic pollutants from wastewater.
 897

898 Acknowledgements

899 The authors gratefully acknowledge the
 900 mechanical faculty of Tabriz University and
 901 the laboratory of the Materials Science and
 902 Engineering Department of Tabriz University.
 903

904 Refrences

905 1. Zhu, L.; Zhou, Y.; Fei, L.; Cheng, X.;
 906 Zhu, X.; Deng, L.; Ma, X. "Z-scheme
 907 CuO/Fe₃O₄/GO heterojunction
 908 photocatalyst: Enhanced
 909 photocatalytic performance for
 910 elimination of tetracycline."
 911 *Chemosphere* 2022, 309 (Pt 2),
 912 136721.
 913 2. Alzuabidi, H. A.; Naghipour, A.;
 914 Fardood, S. T. "Green synthesis and
 915 characterization of Cu_{0.5}Zn_{0.5}FeAlO₄
 916 magnetic nanoparticles with enhanced
 917 photocatalytic activity." *J. Ultrafine
 918 Grained Nanostruct. Mater.* 2024,
 919 158–167.
 920 3. Hu, Y.; Jensen, L.; Schatz, G.
 921 "Photocatalytic reaction pathways on
 922 TiO₂ surfaces: a theoretical study." *J.
 923 Am. Chem. Soc.* 2006, 128, 15734–42.
 924 4. Ge, M.; Cao, C.; Huang, J.; Li, S.;
 925 Chen, Z.; Zhang, K.; et al. "A review
 926 of one-dimensional TiO₂
 927 nanostructured materials for
 928 environmental and energy

929 applications." *Mater. Chem. A* 2016, 4,
 930 6772–6801.
 931 5. Asghar, A.; Aziz, A.; Mohd, A.
 932 "Advanced oxidation processes for in
 933 situ production of hydrogen
 934 peroxide/hydroxyl radical for textile
 935 wastewater treatment: a review." *J.
 936 Cleaner Prod.* 2015, 87, 826–38.
 937 6. Shakir, A. K.; Ghanbari-Adivi, E.;
 938 Baron, A. S.; Soltani, M.
 939 "Investigation of the Effect of
 940 Calcination Time on the Antibacterial,
 941 Antifungal and Anticancer Activities
 942 of TiO₂/ZnO Nanocomposites." *Iran.
 943 J. Mater. Sci. Eng.* 2025, 22 (1).
 944 7. Safavi, M. S.; Bozorg, S.; Ahadzadeh,
 945 I.; Safavi, M. S. "Development of
 946 heterogeneous nano-zeolite catalyzing
 947 Fenton-like oxidation processes for
 948 metalworking fluid wastewater
 949 treatment: A comparison with
 950 conventional methods." *J. Ultrafine
 951 Grained Nanostruct. Mater.* 2024,
 952 190–202.
 953 8. Asai, M. M.; Tapadia, K.
 954 "Biofabricated magnetic CuO@Fe₃O₄
 955 nanocomposites: Synthesis,
 956 characterization and Brilliant Green
 957 dye removal from aqueous media and
 958 its kinetics study." *J. Indian Chem.
 959 Soc.* 2025, 102 (5), 10166.
 960 9. Ajmal, A.; Majeed, I.; Malik, R.;
 961 Idriss, H.; Nadeem, M. "Principles and
 962 mechanisms of photocatalytic dye
 963 degradation on TiO₂-based
 964 photocatalysts: a comparative
 965 overview." *RSC Adv.* 2014, 4, 37003–
 966 26.
 967 10. Soleimani-Amiri, S.; Hossaini, Z.;
 968 Azizi, Z. "Synthesis and investigation
 969 of biological activity of new
 970 oxazinoazepines: Application of
 971 Fe₃O₄/CuO/ZnO@MWCNT magnetic
 972 nanocomposite in reduction of 4-

- 973 nitrophenol in water." *Polycycl.* 1017
 974 *Aromat. Compd.* 2023, 43 (4), 2938– 1018
 975 59. 1019
 976 11. Cruz, M.; Gomez, C.; Duran-Valle, C.; 1020
 977 Pastrana-Martinez, L.; Faria, J.; Silva, 1021
 978 A.; et al. "Bare TiO₂ and graphene 1022
 979 oxide TiO₂ photocatalysts on the 1023
 980 degradation of selected pesticides and 1024
 981 influence of the water matrix." *Appl.* 1025
 982 *Surf. Sci.* 2015, 268, 1–9. 1026
 983 12. Rahmat, R.; Heryanto, H.; Ilyas, S.; 1027
 984 Fahri, A. N.; Mutmainna, I.; Rahmi, M. 1028
 985 H.; Tahir, D. "The relation between 1029
 986 structural, optical, and electronic 1030
 987 properties of composite CuO/ZnO in 1031
 988 supporting photocatalytic 1032
 989 performance." *Desalination Water* 1033
 990 *Treat.* 2022, 270, 289–301. 1034
 991 13. Shen, Y.; Wang, Y.; Chen, Y.; Park, J. 1035
 992 K.; Fang, S.; Feng, K. "Synthesis of 1036
 993 Fe₃O₄/CuO/ZnO/RGO and its 1037
 994 catalytic degradation of dye 1038
 995 wastewater using dielectric barrier 1039
 996 discharge plasma." *Arab. J. Chem.* 1040
 997 2023, 16 (4), 104571. 1041
 998 14. Ohtani, B. "Photocatalysis A to Z – 1042
 999 What we know and what we do not 1043
 1000 know in a scientific sense." *J.* 1044
 1001 *Photochem. Photobiol. C* 2008, 11, 1045
 1002 157–78. 1046
 1003 15. Rashid, H.; Muhammad, E.; Hassan, 1047
 1004 M.; Rauf, A.; Bashir, A.; Ali, W.; et al. 1048
 1005 "Synthesis, structural and 1049
 1006 photocatalytic properties of ZnO-CuO, 1050
 1007 ZnO-Graphene and ZnO-CuO- 1051
 1008 Graphene nanocomposites." 1052
 1009 *Polyhedron* 2025, 273, 117471. 1053
 1010 16. Li, X.; Liu, J.; Liu, E.; Wan, J.; Bai, Z. 1054
 1011 "A review of heterogeneous 1055
 1012 photocatalysts for environmental 1056
 1013 remediation: materials and processes." 1057
 1014 *Chemosphere* 2016, 172, 124–40. 1058
 1015 17. Takahashi, M.; Okada, K.; Malfatti, L.; 1059
 1016 Innocenzi, P. "Formation of interfaces
 responsive and adaptive to
 environment via the sol-gel method."
J. Sol-Gel Sci. Technol. 2024, 112 (1),
 174–81.
 18. Malhotra, A.; Saini, A.; Jindal, N.;
 Kumar, R. "Combustion synthesized
 Fe₃O₄/α-Fe₂O₃/C nanocomposites for
 efficient radiative and non-radiative
 degradation of methylene blue dye."
Inorg. Chem. Commun. 2025, 173,
 113808.
 19. Bopape, D. A.; Hintsho-Mbita, N. C.
 "Commelina benghalensis-mediated
 CuO–ZnO nanocomposite: Effect of
 the pn heterojunction on the
 photocatalytic activity against Congo
 red and carbamazepine." *Inorg. Chem.*
Commun. 2025, 154, 114529.
 20. Intharaksa, O.; Nanan, S.;
 Patdhanagul, N.; Panphojan, T.;
 Srikakul, T.; Tantisuwichwong, N.; et
 al. "Preparation of magnetic
 CuO/Fe₃O₄/ZnO photocatalyst for
 complete degradation of methylene
 blue under natural sunlight
 irradiation." *J. Phys. Chem. Solids*
 2023, 182, 111577.
 21. Melese, A.; Wubet, W.; Abebe, A.;
 Hussen, A. "A comprehensive review
 on recent progress in synthesis
 methods of ZnO/CuO nanocomposites
 and their biological and photocatalytic
 applications." *Results Chem.* 2025, 7,
 102141.
 22. Wahba, M. A.; Yakout, S. M.
 "Microwave-synthesized ZrO₂/ZnO
 heterostructures: fast and high charge
 separation solar catalysts for dyes-
 waste degradation." *J. Sol-Gel Sci.*
Technol. 2022, 104 (2), 330–41.
 23. Ross, J. R. H. "Catalyst
 characterization." In *Contemporary
 Catalysis Fundamentals and Current*

- 1060 *Applications*; 2019; Chapter 5, pp 121– 1103
1061 132.
- 1062 24. Chen, X.; Selloni, A. "Introduction:
1063 Titanium dioxide (TiO₂)
1064 nanomaterials." *Chem. Rev.* 2014, *114*,
1065 9281–82.
- 1066 25. Etay, H.; Kumar, A.; Yadav, O. P.
1067 "Kinetics of photocatalytic
1068 degradation of methylene blue dye in
1069 aqueous medium using ZnO
1070 nanoparticles under UV radiation." *J.*
1071 *Anal. Pharm. Res.* 2023, *12* (1).
- 1072 26. Asli, S. A.; Taghizadeh, M.
1073 "Sonophotocatalytic degradation of
1074 pollutants by ZnO-based catalysts: A
1075 review." *Chem. Select* 2020, 13720–
1076 73.
- 1077 27. Benamara, M.; Nassar, K. I.; Essid, M.;
1078 Frick, S.; Rugmini, R.; Sekhar, K. C.;
1079 Silva, J. P. "Visible light-driven
1080 removal of Rhodamine B using
1081 indium-doped zinc oxide prepared by
1082 sol-gel method." *J. Sol-Gel Sci.*
1083 *Technol.* 2024, *111* (2), 553–65.
- 1084 28. Yuan, N.; Zhang, G.; Guo, S.; Wan, Z.
1085 "Enhanced ultrasound-assisted
1086 degradation of methyl orange and
1087 metronidazole by rectorite-supported
1088 nanoscale zero-valent iron." *Ultrason.*
1089 *Sonochem.* 2016, *28*, 62.
- 1090 29. Khan, M. A. N.; Siddique, M.; Wahid,
1091 F.; Khan, R. "Removal of reactive blue
1092 19 dye by sono, photo and
1093 sonophotocatalytic oxidation using
1094 visible light." *Ultrason. Sonochem.*
1095 2015, *26*, 370–77.
- 1096 30. Taufik, A.; Saleh, R. "Synthesis of iron
1097 (II, III) oxide/zinc oxide/copper (II)
1098 oxide(Fe₃O₄/ZnO/CuO)
1099 nanocomposites and their
1100 photosonocatalytic property for
1101 organic dye removal." *J. Colloid*
1102 *Interface Sci.* 2017, *491*, 27–36.